FWI numerical test using Hussar dataset

Wenyong Pan, Kris Innanen, Gary Margrave, A.Nassir Saeed

ABSTRACT

Full-waveform inversion (FWI) promises high-resolution estimates of subsurface model parameters by iteratively minimizing the difference between the modelled data and observed data. While FWI also suffers from a lot of difficulties, one of which is the cycle-skipping problem resulting from lack of low-frequency and inaccurate initial model. CREWES acquired Hussar low-frequency data set for inversion methods tests. In this paper, we carry out full-waveform inversion tests using the Hussar low-frequency data set.

INTRODUCTION

In September of 2011, CREWES acquired seismic data using different sources (dynamite and vibroseis) and receiver types (10 Hz 3C and 4.5 Hz geophones) for recording low-frequency seismic data down to 2Hz (Margrave et al., 2012). The work was finished with the cooperation of Husky Energy, Geokinetics and INOVA to conduct a unique seismic experiment near Hussar Alberta. A major driver for this research is the understanding that seismic inversion methods, both poststack impedance inversion and full-waveform inversion, require low-frequency information about the desired earth model. A specially modified low-frequency vibrator, the INOVA AHV-IV (model 364), was brought to the experiment by INOVA and a more conventional Failing (Y2400) was rented. The receiver used were Vectorseis 3C(MEMS) accelerometers, 10 Hz SM-7 (ION-sensor) 3C geophones, 4.5 Hz Sunfull 1C geophones, 10 Hz SM-24 high-sensitivity geophones and Nanometrics Trillium seismometers.

Full-waveform inversion (FWI) has emerged as a promising technique for inversing the subsurface parameters by iteratively minimizing a l-2 norm misfit function, which measures the difference between the modelled data and observed data. However, real data application of FWI is impeded by many difficulties including high computation burden, slow convergence rate, cycle-skipping and etc. The cycle-skipping problem results from lack of low-frequency and inaccurate initial model. Hence, the low-frequency information is essential for recovering the long wavelength components of the model and is very important for overcoming the cycle-skipping difficulty. Hussar dataset contains low-frequency information, which is very appropriate for full-waveform inversion tests.

In this paper, we first give a brief description about the Hussar low-frequency data acquisition experiment. Then, we introduce the basic principle of FWI. In the numerical modelling section, we give the inversion result using FWI with the Hussar dataset.

THE EXPERIMENT DESCRIPTION

This experiment was designed by researchers at CREWES in consultation with geophysicists at Husky Energy, Geokinetics, and INOVA. A site near Hussar, Alberta (Figure 1) was chosen primarily because of easy access from Calgary and excellent nearby well control (Margrave et al., 2012). The line location directly ties 3 wells (12-17, 14-27 and

14-35) while two more are nearby. All wells have p-wave sonics, density and gamma ray logs while 12-27 has an shear-wave sonic.

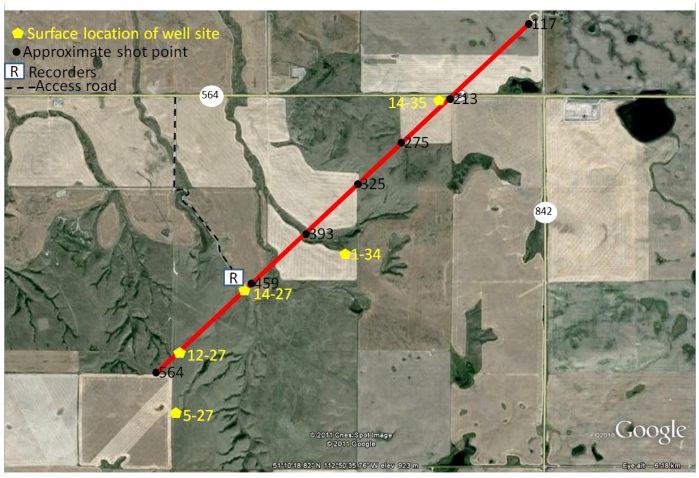

FIG. 1. The 4.5 km Hussar seismic line is shown together with the locations of 5 wells with good logging suites, shotpoint locations, and the location of the recorders (Margrave et al., 2012).

BASIC PRINCIPLE OF FULL-WAVEFORM INVERSION

As a non-linear least-squares optimization problem, the misfit function Φ of FWI is formulated in a least-squares form:

$$\Phi\left(\mathbf{m}\right)=\frac{1}{2}\sum_{\mathbf{x}_s}\sum_{\mathbf{x}_g}\sum_{\omega}\left\|\Delta\mathbf{d}\left(\mathbf{x}_g,\mathbf{x}_s,\omega\right)\right\|^2, \tag{1}$$

where $\mathbf{d}_{obs}$ and $\mathbf{d}_{syn}$ are the recorded data and synthetic data respectively. $\Delta\mathbf{d}=\mathbf{d}_{obs}-\mathbf{d}_{syn}$ is the data residual vector, and $\|\cdot\|$ means the l-2 norm. Here, the synthetic data $\mathbf{d}_{syn}$ is related to the seismic wavefield $\mathbf{u}$ by a detection operator $\mathcal{P}$, which samples the wavefield at the receiver locations: $\mathbf{d}_{syn}=\mathcal{P}\mathbf{u}$. The Newton optimization approach is developed based on the second-order Taylor-Lagrange expansion of the misfit function Φ:

$$\Phi\left(\mathbf{m}+\Delta\mathbf{m}\right)\approx\Phi\left(\mathbf{m}\right)+\mathbf{g}^{\dagger}\Delta\mathbf{m}+\frac{1}{2}\Delta\mathbf{m}^{\dagger}\mathbf{H}\Delta\mathbf{m}, \tag{2}$$

where the symbol "†" means transpose, $\Delta\mathbf{m}$ is the search direction, $\mathbf{g}=\nabla_{\mathbf{m}}\Phi\left(\mathbf{m}\right)$ and $\mathbf{H}=\nabla_{\mathbf{m}}\nabla_{\mathbf{m}}\Phi\left(\mathbf{m}\right)$ indicate gradient and Hessian respectively.

To minimize the quadratic approximation of the misfit function, the updated model at the $(k+1)$th iteration can be written as the sum of the model at the kth iteration and the search direction $\Delta\mathbf{m}_k$:

$$\mathbf{m}_{k+1}=\mathbf{m}_k+\mu_k\Delta\mathbf{m}_k, \tag{3}$$

where μ_k is the step length, a scalar constant calculated through a line search method satisfying the weak Wolfe condition (Gauthier et al., 1986; Pica et al., 1990; Nocedal and Wright, 2006). Within a Newton optimization framework, the search direction $\Delta\mathbf{m}_k$ is the solution of the Newton linear system:

$$\mathbf{H}_k\Delta\mathbf{m}_k=-\mathbf{g}_k. \tag{4}$$

The gradient is the first-order partial derivative of the misfit function with respect to the model parameter and it indicates the direction in which the misfit function is increasing most rapidly (Pratt et al., 1998). It can be constructed by zero-lag correlation between the Fréchet derivative wavefield with complex conjugate of the data residuals $\Delta\mathbf{d}$:

$$\mathbf{g}(\mathbf{x}) = \nabla_{\mathbf{m}(\mathbf{x})}\Phi(\mathbf{m}) = -\sum_{\mathbf{x}_g}\sum_{\mathbf{x}_s}\sum_{\omega}\Re\left(\frac{\partial\mathbf{d}^{\dagger}_{syn}(\mathbf{x}_g,\mathbf{x}_s,\omega)}{\partial\mathbf{m}(\mathbf{x})}\Delta\mathbf{d}^{*}(\mathbf{x}_g,\mathbf{x}_s,\omega)\right), \quad (5)$$

where the symbol "$*$" means complex conjugate, $\frac{\partial\mathbf{d}_{syn}(\mathbf{x}_g,\mathbf{x}_s,\omega)}{\partial\mathbf{m}(\mathbf{x})}$ indicates the Fréchet derivative wavefield (or Jacobian matrix) recorded at the receiver $\mathbf{x}_g$ due to model perturbation at position $\mathbf{x}$ and $\Re(\cdot)$ denotes the real part. Within the adjoint-state formalism (Plessix, 2006), the gradient can be expressed as (Sirgue and Pratt, 2004; Plessix and Mulder, 2004; Tao and Sen, 2013; Pan et al., 2015a):

$$\mathbf{g}(\mathbf{x}) = \sum_{\mathbf{x}_g}\sum_{\mathbf{x}_s}\sum_{\omega}\Re\left(\omega^2 f_s(\omega)\,G(\mathbf{x},\mathbf{x}_s,\omega)\,G(\mathbf{x}_g,\mathbf{x},\omega)\,\Delta\mathbf{d}^{*}(\mathbf{x}_g,\mathbf{x}_s,\omega)\right), \quad (6)$$

where $G(\mathbf{x},\mathbf{x}_s,\omega)$ and $G(\mathbf{x}_g,\mathbf{x},\omega)$ indicate source-side and receiver-side Green's functions respectively. Following equation (6), the gradient can be constructed efficiently by cross-correlating the forward modelled wavefield with the back-propagated data residual wavefield (Virieux and Operto, 2009; Pan et al., 2015b,c). The gradient is poorly-scaled due to geometrical spreading, and it is also contaminated by spurious correlations because of finite-frequency effects and doubly-scattered energy (Pratt et al., 1998). The Hessian operator is the second-order partial derivative of the misfit function with respect to the model parameter (Pratt et al., 1998; Plessix and Mulder, 2004):

$$\begin{aligned}\mathbf{H}(\mathbf{x},\mathbf{x}') &= \nabla_{\mathbf{m}(\mathbf{x})}\nabla_{\mathbf{m}(\mathbf{x}')}\Phi(\mathbf{m})\\ &= \sum_{\mathbf{x}_g}\sum_{\mathbf{x}_s}\sum_{\omega}\Re\left(\frac{\partial\mathbf{d}^{\dagger}_{syn}(\mathbf{x}_g,\mathbf{x}_s,\omega)}{\partial\mathbf{m}(\mathbf{x})}\frac{\partial\mathbf{d}^{*}_{syn}(\mathbf{x}_g,\mathbf{x}_s,\omega)}{\partial\mathbf{m}(\mathbf{x}')} + \frac{\partial^2\mathbf{d}^{\dagger}_{syn}(\mathbf{x}_g,\mathbf{x}_s,\omega)}{\partial\mathbf{m}(\mathbf{x})\,\partial\mathbf{m}(\mathbf{x}')}\Delta\mathbf{d}^{*}(\mathbf{x}_g,\mathbf{x}_s,\omega)\right),\end{aligned} \quad (7)$$

where $\mathbf{x}'$ is the neighboring position around the position $\mathbf{x}$ (Valenciano, 2008; Pan et al., 2015a) and $\frac{\partial^2\mathbf{d}_{syn}(\mathbf{x}_g,\mathbf{x}_s,\omega)}{\partial\mathbf{m}(\mathbf{x})\partial\mathbf{m}(\mathbf{x}')}$ means the second-order partial derivative wavefield due to model perturbations at positions $\mathbf{x}$ and $\mathbf{x}'$. Multiplying the gradient with the inverse Hessian can greatly enhance the model update, which provides a quadratic convergence rate.

NUMERICAL EXPERIMENT

The shot gathers are generated by Saeed et al. (2014). Figures 2a and 2b show the shot gathers after pre-processing. Figure 3a shows the initial velocity model used for FWI, which is actually obtained by traditional velocity analysis. Figure 3a shows the gradient update with the frequency band of (1-3) Hz. Figure 3 shows the inverted model at the first iteration. Figures 4a, 4b and 4c show the inverted models at the 4th, 6th and 10th iteration respectively. As we can see, the resolution of the velocity model is enhanced as the iteration proceeds. Figures 4d, 4e and 4f show the corresponding reverse time migration imaging results. It is noticed that inverted models give better imaging results.

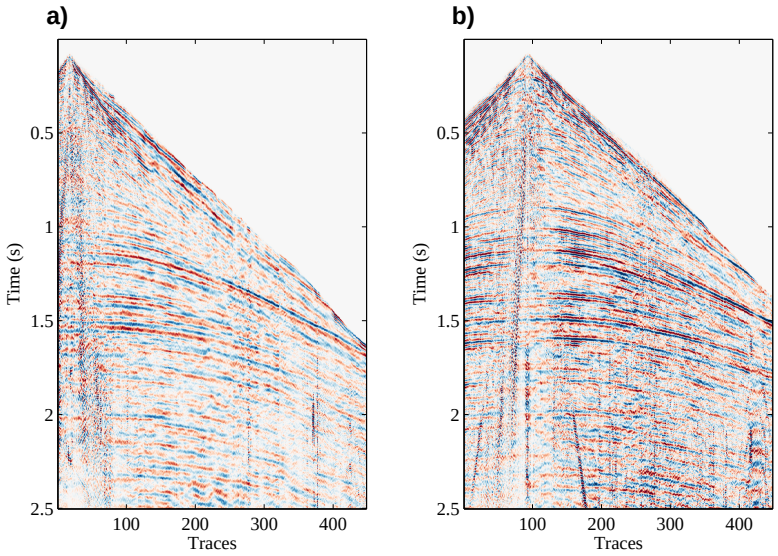

FIG. 2. Shots after pre-processing. (a) shot 18; (b) shot 100.

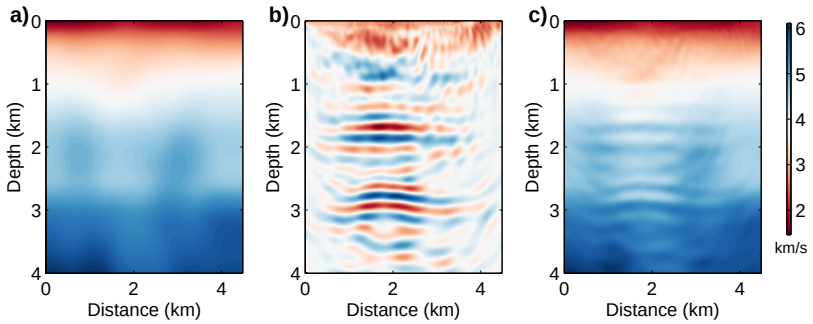

FIG. 3. (a) Initial model; (b) Gradient update; (c) Updated model at the 1st iteration.

CONCLUSION

In this paper, we perform the full-waveform inversion test using the Hussar low-frequency dataset. We demonstrate that with the inverted velocity model, the reverse time migration imaging result is improved.

ACKNOWLEDGEMENTS

The authors thank the sponsors of CREWES for continued support. This work was funded by CREWES industrial sponsors and NSERC (Natural Science and Engineering Research Council of Canada) through the grant CRDPJ 461179-13. Author 1 was also supported by a SEG/Chevron scholarship.

REFERENCES

Gauthier, O., Virieux, J., and Tarantola, A., 1986, Two-dimensional nonlinear inversion of seismic waveforms: numerical results: Geophysics, **51**, 1387–1403.

Margrave, G. F., Mewhort, L., Phillips, T., Hall, M., Bertram, M. B., Lawton, D. C., Innanen, K., Hall, K. W., and Bertram, K., 2012, The hussar low-frequency experiment: CSEG Recorder, 25–39.

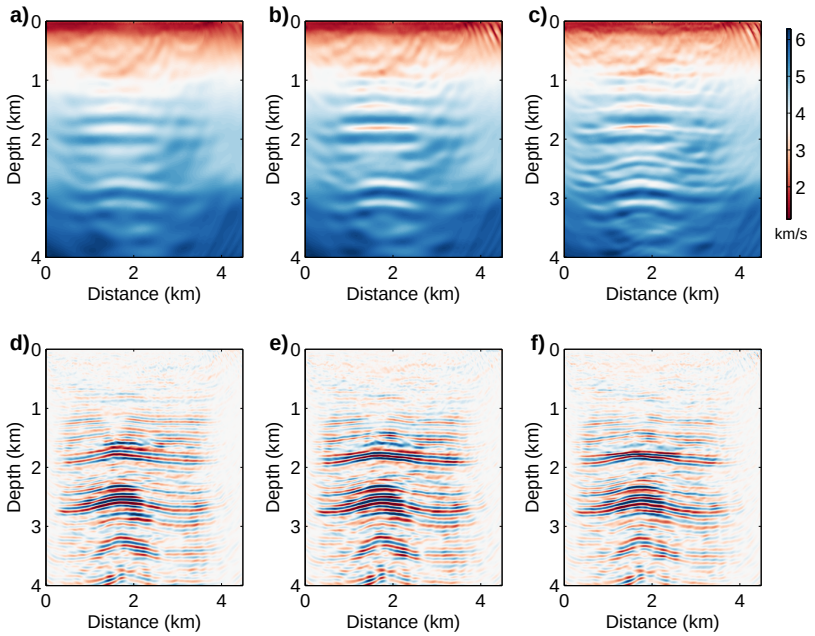

FIG. 4. (a), (b) and (c) show the inversion results at 4th, 6th and 10th iterations. (d), (e) and (f) show the reverse time migration images using the corresponding inverted models.

Nocedal, J., and Wright, S. J., 2006, Numerical Optimization: Springer.

Pan, W., Innanen, K. A., Margrave, G. F., and Cao, D., 2015a, Efficient pseudo-Gauss-Newton full-waveform inversion in the τ-p domain: Geophysics, **80**, R225–R14.

Pan, W., Innanen, K. A., Margrave, G. F., Fhler, M. C., Fang, X., and Li, J., 2015b, Estimation of elastic constants in HTI media using Gauss-Newton and Full-Newton multi-parameter full-waveform inversion: SEG Technical Program Expanded Abstracts, 1177–1182.

Pan, W., Innanen, K. A., Margrave, G. F., Fhler, M. C., Fang, X., and Li, J., 2015c, Estimation of elastic constants in HTI media using Gauss-Newton and Full-Newton multi-parameter full waveform inversion: Geophysical Journal International, Submitted.

Pica, A., Diet, J. P., and Tarantola, A., 1990, Nonlinear inversion of seismic reflection data in a laterally invariant medium: Geophysics, **55**, 284–292.

Plessix, R. E., 2006, A review of the adjoint-state method for computing the gradient of a functional with geophysical applications: Geophysical Journal International, **167**, 495–503.

Plessix, R. E., and Mulder, W. A., 2004, Frequency-domain finite-difference amplitude-preserving migration: Geophysical Journal International, **157**, 975–987.

Pratt, R. G., Shin, C., and Hicks, G. J., 1998, Gauss-Newton and full Newton methods in frequency-space seismic waveform inversion: Geophysical Journal International, **133**, 341–362.

Saeed, N., Margrave, G. F., Henley, D. C., Isaac, J. H., and Lines, L. R., 2014, Seismic imaging of the hussar low frequency seismic data: CREWES Annual Report, 1–18.

Sirgue, L., and Pratt, R. G., 2004, Efficient waveform inversion and imaging: A strategy for selecting temporal frequencies: Geophysics, **69**, 231–248.

Tao, Y., and Sen, M. K., 2013, Frequency-domain full waveform inversion with plane-wave data: Geophysics, **78**, R13–R23.

Valenciano, A., 2008, Imaging by wave-equation inversion: Ph.D. thesis, Stanford University.

Virieux, A., and Operto, S., 2009, An overview of full-waveform inversion in exploration geophysics: Geophysics, **74**, WCC1–WCC26.